Experimental Characterization of the Flow-Induced Flutter of a Suspended Elastic Membrane

Zhongwang Dou[1], Aaron Rips[2], Lauren Jacob[3], and Rajat Mittal[4]
Johns Hopkins University, Baltimore, MD, 21218, USA

Flow-induced flutter (FIF) of elastic membranes has many applications in engineering, biology and medicine, and recent advances in computational modeling are enabling simulation of such problems in unprecedented detail. However, appropriate experiments that would allow comprehensive validation of such models is lacking. To fill this gap, we conduct low Reynolds number experiments on the flow-induced flutter of a suspended elastic membrane. This configuration has well defined boundary conditions and exhibits a variety of flutter regimes, thereby making it a suitable case for validation. Silicon sheets of three different thicknesses are used as the material for the suspended membrane and the other key variables in the study are the flow speed and the yaw angle of the membrane. The deflection and flutter motion of each membrane is measured using a high-speed imaging system. A variety of flutter regimes are observed for the parameters studied here, including nominally two-dimensional flutter as well as highly three-dimensional motion for non-zero yaw angles. Qualitative as well as quantitative features of the flutter are catalogued in order to provide a comprehensive dataset for validation.

Nomenclature

L, W, h	=	Membrane length, width, and thickness
U	=	Flow velocity
ρ_m, ρ_f	=	Density of membrane, density of air
m	=	Mass of membrane

[1] Postdoctoral Fellow, Department of Mechanical Engineering; Currently Postdoc at Purdue University.
[2] Graduate Student, Department of Mechanical Engineering.
[3] Undergraduate Student, Department of Mechanical Engineering.
[4] Professor, Department of Mechanical Engineering, AIAA Associate Fellow; Corresponding Author: mittal@jhu.edu.

ν	=	Air kinematic viscosity
g	=	Gravitational constant
E	=	Young's modulus
k_b	=	Flexural rigidity
θ_Y	=	Yaw angle
Φ	=	Banner deflection angle
Φ_{mean}	=	Mean of banner deflection angle
Φ_{RMS}	=	Root mean square of banner deflection angle
f_Φ	=	Banner flutter frequency
St	=	Strouhal number

I. Introduction

Flow-induced flutter (FIF) features in a variety of engineering applications including aircraft wings and control surfaces[1], helicopter rotors [2], biological and bioinspired locomotion in fluid (swimming and flying) [3, 4], physiological flows (such as heart valves and vocal fold vibration)[5], heat transfer enhancement [6], and piezo electric energy harvesting [7], just to name a few. Furthermore, FIF of highly flexible bodies such as thin membranes presents rich, coupled dynamics that not only serve as configurations for experimental study of nonlinear dynamical phenomena, they also pose significant challenges for computational modeling and simulation. Over the past two decades a number of fluid-structure interaction (FSI) simulation techniques have been developed to model these complex multi-physics systems [8-17]. However, for the most part, such modeling efforts have proceeded without strong quantitative validation. Even in studies where some degree of validation has been demonstrated it has been limited to a very small number of conditions in the parameter space of the problem and comparisons to experiments are mostly qualitative. For example, studies in Refs. [18-23] modeled a single flag, and compared the shape of the flapping envelopes and the flapping amplitude with the soap film experiments of Zhang*, et. al.* [24]. Studies in Refs. [25-29] modeled multiple conventional flags and compared the phase shift coupling behavior with Zhang*, et. al.* [24]. The study of Ryu*, et. al.* [30] compared the simulated flapping behavior of an inverted flag with the experiments of Kim*, et. al.* [31].

Some modeling studies have employed comparisons with other simulations as a way to verify the accuracy of their models. For example, Gurugubelli and Jaiman [32] cross-verified their simulations of a 2D conventional flag configuration with the simulations of Connell and Yue [33]. Shoele and Mittal [34] used Turek and Hron [35] simulations of flutter of a flexible plate mounted behind a circular cylinder, to verify their FSI model. Tang, *et. al.* [36] and Dong, *et. al.* [37] cross-verified their 3D conventional flag simulations against those of Huang and Sung [20].

There are few FIF simulations that have performed quantitative validation against experiments. One example is the work of Gilmanov, *et. al.* [38] who compared the leading-edge displacement of a rectangular inverted flag against the experimental measurements of Kim, *et. al.* [31] and found a good match. However, this comparison was for a single case, and it is unclear the degree to which the compared quantity is sensitive to system parameters such as Reynolds number and bending stiffness. Thus, systematic validation of computational models over a range of system parameters, which would provide the required level of confidence in the computational models, are, to the best of our knowledge, missing.

To a large degree, this lack of validation is related to the unavailability of experiments that are well-suited for computational validation. Existing experiments of FIF in canonical elastic membranes can be roughly classified in three configurations: conventional flags, bending membranes and inverted flags. The conventional flag configuration has the membrane inline with the incoming flow, with a clamped leading edge and a free trailing edge. Taneda [39] performed one of the first experiment of a paper flag in a wind tunnel and obtained the flutter modes, velocity, frequency, and drag on the flag. Yamaguchi, *et. al.* [40] tested the flutter of thin flexible sheets with different mass ratios using an optical laser frequency analyzer. Zhang, *et. al.* [24] demonstrated the flutter of a flexible filament in a soap film apparatus and studied the coupling of flag motion with the hydrodynamics. The aeroelastic instability of conventional flags has been discussed extensively [41-46], including its application to energy harvesting [7, 45, 47-56]. In bending membrane configurations, the membrane surface is oriented perpendicular to the flow, and clamped across the middle. Research in this configuration has been motivated in some part by flow-induced deformation of leaves and sea grasses, and axisymmetric swimmer [57-60]. The inverted flag configuration is a relatively new one; it has a membrane aligned with the flow, but with a free leading-edge and a clamped trailing-edge. Kim, *et. al.* [31] and Sader, *et. al.* [61] and subsequently, a number of other groups have used experiments and simulations to explore various aspects of this configuration [7, 22, 23, 30, 32, 36, 56, 62, 63].

From the perspective of validating computational models, the following are the desirable features of a FIF experiment:

a) The configuration should be "canonical," i.e. relatively simple, with a limited set of parameters, and yet, capable of exhibiting a wide range of physical phenomena.

b) The FIF phenomena should occur over a broad range of Reynolds numbers, ranging from low O(1000) to >O(10^5) so as to allow validation of a range of simulations methodologies such as direct numerical simulation (DNS), large-eddy simulation (LES) and even Reynolds-averaged Navier Stokes (RANS) simulation. Obtaining robust flutter on the lower end of this Reynolds number range is however, particularly difficult since flutter usually occurs at relatively high flow speeds and for large membranes [31, 43, 54, 64-67].

c) The configuration should generate considerable three-dimensional effects and yet be reducible to a nominally two-dimensional configuration to enable the deployment of inexpensive 2D models.

d) The material properties of the fluttering element, and the boundary conditions for the flow as well as the fluttering element, should be defined and cataloged in a precise manner.

e) Experiments should measure a sufficient set of quantities associated the fluttering element (frequency, mode shapes, amplitudes, etc.) over a wide range of system parameters so as to enable comprehensive validation.

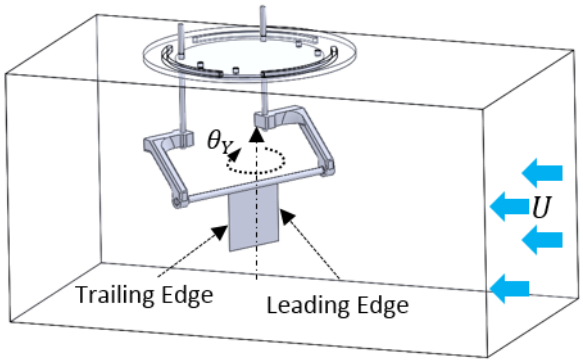

Figure 1. Schematic of suspended membrane configuration inside the test-section of the wind-tunnel.

The current study is motivated primarily by this need for an experimental dataset suitable for validation of FIF simulations. We propose a new configuration for this purpose: a rectangular elastic membrane suspended from a horizontal support in a parallel, uniform flow (U) with adjustable yaw angle (θ_Y), illustrated in Fig. 1. The primary dimensionless numbers that describes the FIF of this configuration are:

Membrane aspect ratio: $AR = W/L$

Reynolds number: $Re = UL/\nu$

Froude Number: $Fr = U/\sqrt{gL}$

Mass Ratio: $M^* = (\rho_f/\rho_m)L/h$

Reduced velocity: $U^* = UL\sqrt{\rho_m h/k_b}$

Here L, W and h are the length, width and thickness of the rectangular membrane respectively, U and ν are the inlet flow speed and fluid kinematic viscosity, respectively, ρ_f and ρ_m are the densities of the fluid and the membrane, respectively, and g is the acceleration due to gravity. Furthermore, k_b is the flexural rigidity of the membrane and is given by $k_b = Eh^3/12(1 - v_p^2)$, where E and v_p are the Young's modulus and Poisson's ratio of the membrane material, respectively.

This configuration has well-defined boundary conditions, is capable of generating both two- and three-dimensional flutter, and is expected to generate a wide range of flutter behaviors that would be useful for validation. We implement this "suspended membrane" setup in a low Reynolds number wind-tunnel and characterize the flutter behavior using high-speed videogrammetry. In addition to the material parameters of the membrane, we quantify the effect of flow speed and the yaw angle of the membrane on the kinematics of flutter.

II. Experiment Configuration

A. Experimental Setup

The experiment is conducted in an open-return, low Reynolds number wind tunnel shown in Fig. 2a. The wind tunnel system consists of an inlet with a contraction section (1:9 area contraction ratio), a $12'' \times 12'' \times 24''$ test section, and a downstream diffuser with a $18''$ fan. The fan (Cincinnati Fan 18-6-35), is driven by a three-phase, 0.75 hp AC motor (Baldor M3542) producing a maximum flow volume flow rate of 4000 CFM. An AC motor VFD (Variable Frequency Drive, ABB ACS150) is employed to vary the flow speed in the test section directly. Flow straighteners in the inlet of the contraction (honeycomb with diameter of $0.5''$), as well as the inlet and outlet of the test section (honeycomb with diameter of $0.125''$), are employed to obtain a uniform flow as well as to reduce the turbulence intensity in the test section. The flow inside the test section is characterized using a hot-wire anemometer (Testo 301) and found to be sufficiently homogeneous. The measured air speed in the test section ranges from 0.1 -

18.4 m/s, and the turbulence intensity is measured to be below 0.5%. A high-speed CMOS camera (IDT Y4-S1, 1016 × 1016 pixels, 12 μm/pixel) is employed to record the motion of the membrane under the illumination of a 250 Watt halogen lamp, shown in Fig. 2a and 2c.

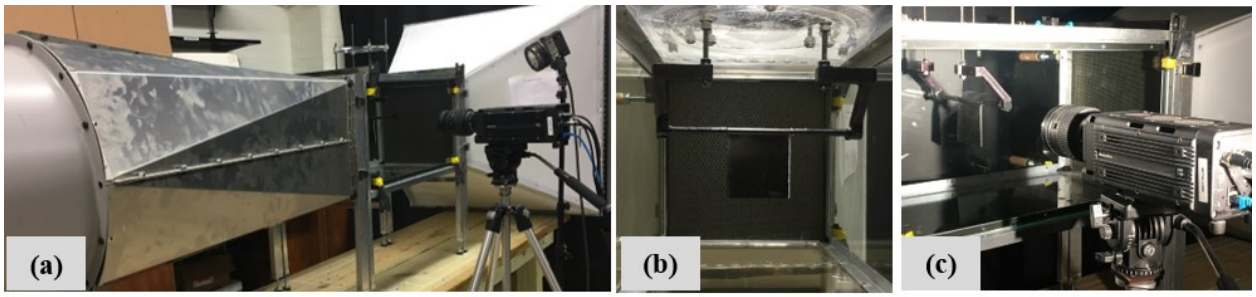

Figure 2. Experimental setup when Yaw angle = 0°. (a) The low Reynolds number wind tunnel; (b) Silicone membrane coated with black and white at edge, suspended in the test section; and (c) high-speed camera used to record the membrane flutter.

Silicon sheets (Fullchance Industrial Co. Ltd.) with three different thicknesses (h = 0.62, 0.79, and 0.92 mm) are employed as the membrane material. These silicon sheets have densities of $\rho_m = 1.194 \times 10^3$, 1.170×10^3 and 1.304×10^3 kg/m^3 for the 0.62, 0.79 and 0.92 mm membranes, respectively. The Young's modulus of these silicone sheets are characterized using dynamic testing with a rheometer (Anton-Paar Inc., MCR 302) which is better suited for this study firstly because silicon sheets are viscoelastic and secondly, because the study involves dynamic (and not static) deformation induced by fluttering. Thus, the material properties extracted from these dynamic tests are expected to be more appropriate than those obtained from static tension tests.

By sweeping the amplitude of the applied strain on the rheometer at a frequency of 5 rad/s, the shear loss (G_{loss}) and shear storage ($G_{storage}$) modulus of the silicon sheet are returned. Finally, the Young's modulus (E) is estimated (Fig. 3) by using the specified Poisson's ratio of v_p =0.48 for these sheets and the following well-established [68] relationship: $E = 2(1 + v_p) \cdot \left(G_{loss}^2 + G_{storage}^2\right)^{0.5}$). We also performed a frequency sweep with the rheometer from 1 – 100 rad/s at a strain amplitude of 5% and found that the modulus varied by less than 10%. The flexural rigidity(k_b) of each membrane at low strain rate (0.01%) is then estimated to be 2.53×10^{-5}, 4.64×10^{-5}, and 11.21×10^{-5} $N \cdot m$ for the 0.62, 0.79, and 0.92 mm membranes, respectively.

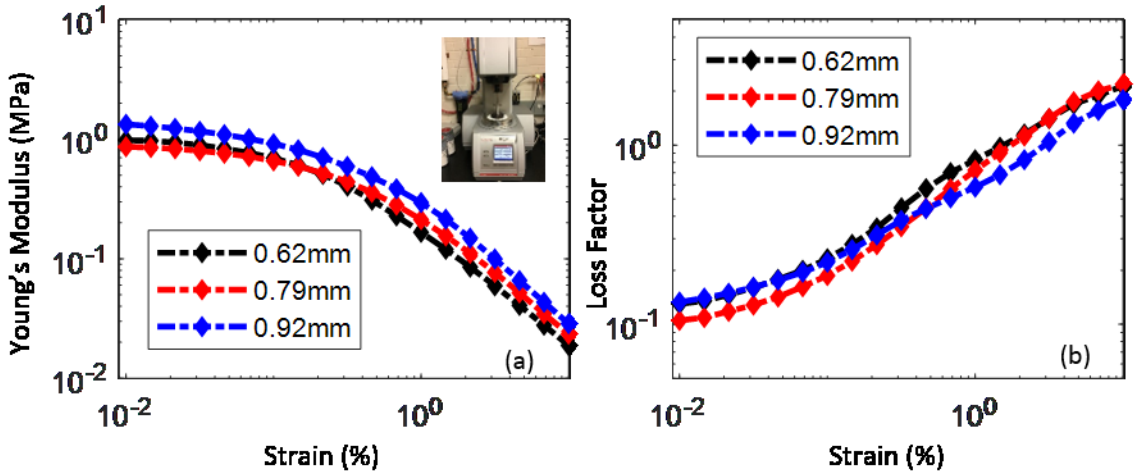

Figure 3. Membranes properties measured over a range of strain amplitudes using a rheometer (inset). (a) Young's modulus, (b) Loss factor.

B. Experimental Conditions

Experiments are conducted for square membranes with $L = W = 75\ mm$. This membrane is large enough to generate significant flutter at the wind speeds available in the wind-tunnel but small enough to occupy less than 10% of the cross-sectional area of the tunnel test section. The surface of the membrane is painted black and the edges of membrane are marked with white paint to enhance the visibility of membrane motion. The membrane is clamped by a cylindrical holder (6.35 mm diameter) and held vertically by a mounting system. This mounting system can adjust the yaw-angle (θ_Y) from 0 (membrane surface normal to flow) to 90 degrees (membrane surface parallel to the flow). All of these tests were conducted at room temperature (20° C).

Table 1. Test conditions for the first set of cases that examine the effect of membrane thickness, flow velocity and yaw angle on flow-induced flutter. Further details are in the Appendix.

Membrane Thickness ($\boldsymbol{mm}$)	Yaw angle (degree)	Flow Velocity ($\boldsymbol{m/s}$)
0.62	0	0.0 → 18.4
0.62	45	0.0 → 18.4
0.79	0	0.0 → 18.4
0.79	45	0.0 → 18.4
0.92	0	0.0 → 18.4
0.92	45	0.0 → 18.4

We first test the deflection and flutter phenomena of the membrane at different flow speeds. The flow speed of the wind tunnel is controlled by a VFD, and increasing the VFD output with 5 Hz increments results in velocity increments

of 0.5 - 1.2 m/s (this increment gradually increases when the driving frequency increases from 0 Hz, and it reaches a plateau at a driving frequency of 30 Hz). Once flutter is observed, the increment is reduced to 2.5 Hz in order to obtain finer scale details of the flutter phenomenon. Furthermore, a limited number of measurements with 1 Hz increments are also conducted around the primary bifurcation. Table 1 tabulates all the test conditions for these initial set of experiments. The highest flow velocity in the current experiments is 18.4 m/s and this corresponds to a Reynolds number of 9.1×10^4.

For the zero yaw angle case ($\theta_Y = 0°$), the flutter is nominally two-dimensional and only one side of the edge is recorded. For $\theta_Y = 45°$, the motion of both the leading and trailing-edges are recorded. Under each test conditions, we record the membrane motion at 200 frames per second (FPS) before flutter and 1000 FPS after the onset of flutter. These high-speed videos are then post-processed using the method described in section 2.3 below. Six independent experiments are conducted at each condition and quantities such as mean flutter amplitude and frequencies are ensemble averaged over these experiments. The results are presented in Section 3.1 and 3.2 below.

The second set of experiments address the effect of membrane size and aspect-ratio on the onset of flutter and the key parameters for these experiments are tabulated in Table 2. Starting with the baseline membrane of size 75 mm $\times$ 75 mm, in the first subset of experiments, the membrane length is kept at 75 mm and the membrane width is decreased of the membrane with a decrement of 5 mm down to a final width of 5 mm. In the second subset, the membrane width is kept at 75 mm and the length of the membrane is decreased in decrements of 5 mm. Finally, we quantify the effect of membrane aspect-ratio on the critical speed by employing four membranes that have the same total surface area as the baseline membrane but different aspect ratios: 37.5 $\times$ 150 mm, 50 $\times$ 112.5 mm, 75 $\times$ 75 mm (baseline), and 112.5 $\times$ 50 mm. These conditions are documented in Table 2. We measure the critical speed (i.e. flow speed at the onset of flutter) for each of these membranes and the results are presented in Section 3.3.

Table 2. Test conditions for critical speed measurement for $\theta_Y = 0°$

Membrane thickness (mm)	Constant parameter	Changing parameter
0.62	$L = 75$ mm	$W = 75, 65, 60, 55, 50, 45, 40, 30, 25, 20, 15, 10, 5$ mm
0.79	$W = 75$ mm	$L = 75, 70, 65, 60, 55, 50, 45, 40$ mm
0.62	$L \times W = 5625$ mm^2	$AR = W/L = 0.25, 0.44, 1, 2.25$

C. Imaging and Data Analysis

As mentioned above, the surface of the membranes is painted black and edges are painted white for contrast. A single snapshot of the fluttering membrane is shown in Fig. 4a. Automated detection and tracking of the edge of the membrane is accomplished via a customized MATLAB code [69-71]. The detected edge of the membrane is segmented into 20 equally spaced increments and by repeating this procedure for each frame of the recorded high-speed video, we can reconstruct the trajectory of the various points on the membrane as demonstrated in Fig. 4d and 4e. The mean amplitude of tip flutter in the vertical direction (A_{tip} in Fig. 4e) can be estimated in a straightforward manner. We reconstruct the membrane's envelope for each case with an increment of 0.005 seconds. The point on the tip of the membrane edge is particularly important and the speed of tip movement is also calculated based on the tip displacement between frames. Given that many cases, especially at high flow speeds exhibit cycle-to-cycle variations, we compute a phase average of the tip trajectory at four flow speeds for 0.62 membrane in order to provide a qualitative view of the membrane flutter. These results are shown in Section 3.1.

For quantitative characterization of the flutter, we focus on a single measured parameter, the angle (Φ), subtended by the tip of the membrane edge from the vertical axis (see Fig. 4f). This parameter is tracked over time during each experiment and the overall deflection of the membrane, flutter amplitude and flutter frequency are then represented by the quantities Φ_{mean} (mean value), Φ_{RMS} (root-mean-square value) and f_{Φ} (dominant frequency identified in the Fourier spectrum of the time series of Φ), respectively. We quantify the flutter in terms of these three parameters for the cases studied here and these results are presented in section 3.2.

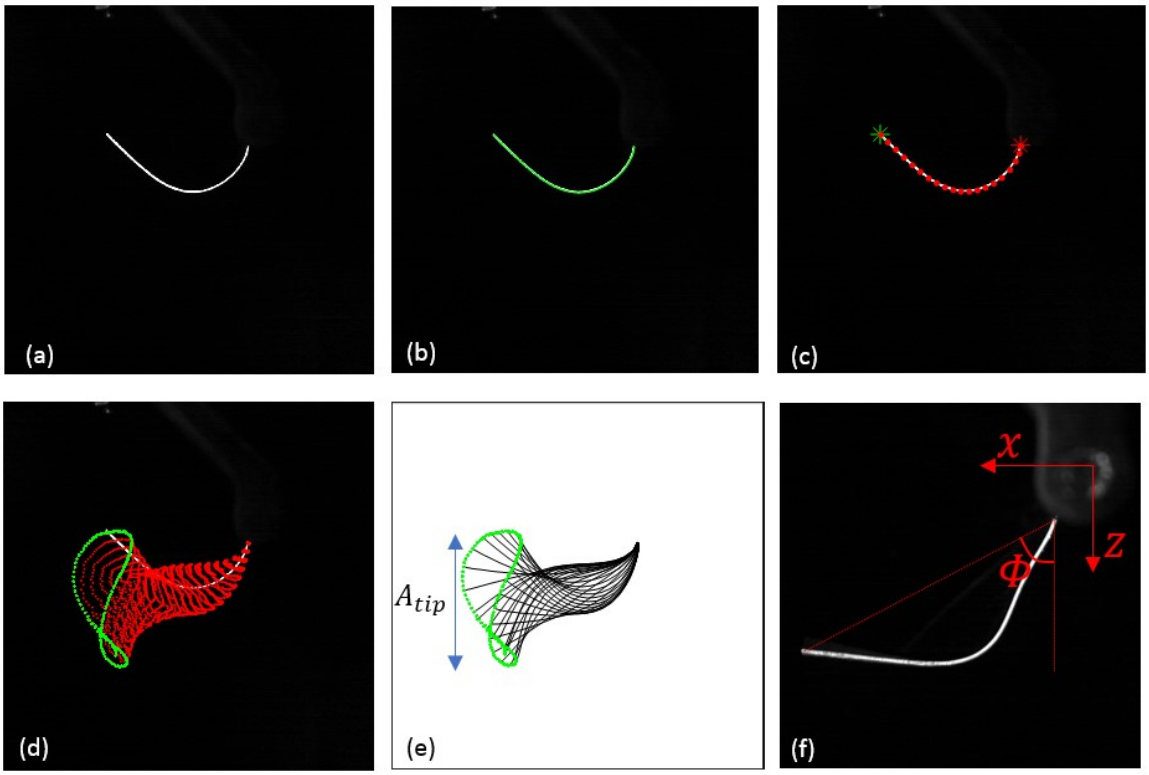

Figure 4. Data and imaging for 0.79 mm thickness membrane at flow speed of 7.8 m/s. (a) Raw image of a fluttering membrane from the high-speed camera (b) reconstruction of membrane edge shape through automated edge-detection; (c) edge segmented into 20 equal segments with membrane tip and root identified; (d) flutter pattern reconstruction over 0.15ms. Green line shows the trajectory of the membrane tip; (e) flutter envelope over 0.15s indicating the tip amplitude A_{tip}; (f) Estimation of deflection angle Φ at one time-instance.

III. Results

A. FIF Envelope and Membrane Trajectories

The FIF envelope at four flow speeds for the 0.62 mm membrane for yaw angles of zero (no yaw) and 45° shown in Fig. 5 provides a qualitative view of the flutter behavior. The selected flow speeds correspond to the following conditions: (1) slightly before the onset of flutter; (2) immediately after the onset of flutter; (3) intermediate speed beyond the critical speed and (4) high flow speed. For the zero yaw angle case, the flutter is mostly two-dimensional and we therefore show the data only for one edge. For the 45° yaw angle case, the flutter motion is highly three-dimensional and we provide data on both the leading and trailing edges of the membrane.

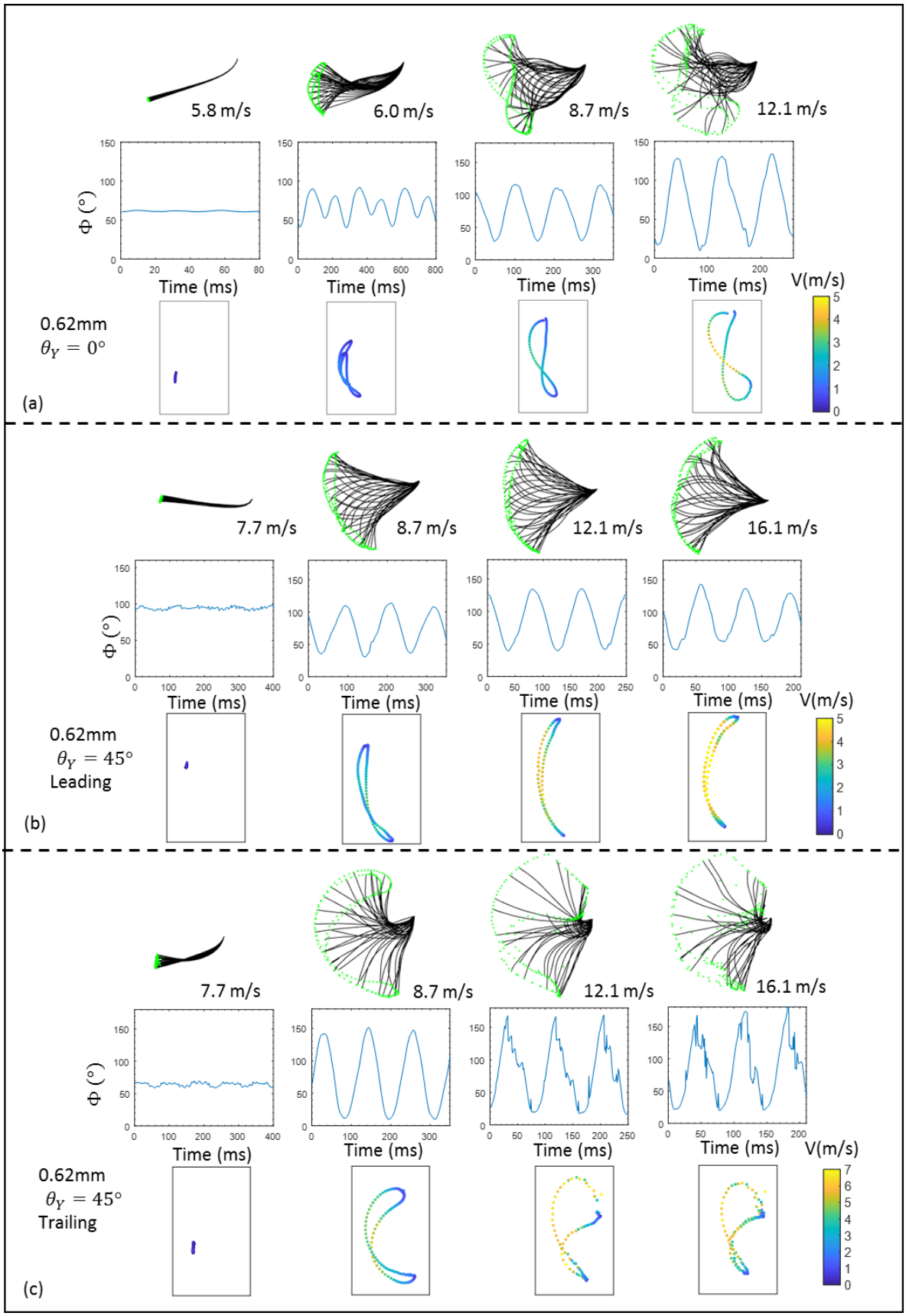
5.8 m/s
6.0 m/s
8.7 m/s
12.1 m/s
Φ (°)
Time (ms)
V(m/s)
0.62mm
$\theta_Y = 0°$
(a)
7.7 m/s
8.7 m/s
12.1 m/s
16.1 m/s
0.62mm
$\theta_Y = 45°$
Leading
(b)
7.7 m/s
8.7 m/s
12.1 m/s
16.1 m/s
0.62mm
$\theta_Y = 45°$
Trailing
(c)

Figure 5. Envelope, deflection angle versus time, and phase-averaged tip trajectory of 0.62mm membrane at different flow speeds and yaw angles. (a) Yaw angle $\theta_Y = 0°$. (b) Leading-edge for yaw angle $\theta_Y = 45°$, and (c) trailing-edge for yaw angle $\theta_Y = 45°$. Envelopes are plotted for membrane flutter over a duration of 0.15 s at 0.005 s time increments. Below each envelope is shown the corresponding plot of Φ versus time over three cycles. Phase averaged trajectories were obtained and the velocity of each is encoded in the color. These tip trajectories are drawn to scale: vertical and horizontal sizes of the picture frame correspond to 11 and 7 cm, respectively.

Before the onset of large amplitude flutter, the membrane exhibits small amplitude movements. However, once the flow speed slightly exceeds the critical value, highly periodic flutter phenomena is observed with the tip of the membrane edge executing a "figure-8" motion. One exception is the $\theta_Y = 0°$ case with the velocity of 6.0 m/s, which shows a complex trajectory with multiple loops and this is indicative of the presence of a subharmonic frequency in the movement. In general, the amplitude of this motion increases with flow-speed and for the higher flow speeds, we observed complex kinematics which include membrane buckling and snapping. Furthermore, in order to provide a qualitative view of the flutter phenomena, we reconstruct the phase-averaged tip trajectory for each membrane in Fig. 5 as well. The color in each trajectory represents the tip speed, and the movement direction is clockwise in the loop of the "figure 8" shape and counter clockwise in the lower loop. For the 45° yaw-angle case, the movement of the leading and trailing edges remains quite distinct over the entire range of flow velocities. We provide videos of reconstructed flutter motion in the supplementary material.

B. Membrane Flutter versus Flow Speed

Figure 6 shows the trends in mean deflection, flutter amplitude and flutter frequency for all the baseline (square) membrane cases. The standard deviation between the six individual experiments for each case is included in all these plots.

A number of observations can be made from these plots. First, for all the three membranes at zero yaw angle (i.e. $\theta_Y = 0°$), we can identify distinct regimes with increasing flow velocity. For the case of the 0.62 mm membrane, the first regime extends from the lowest speed to about 6 m/s. In this regime Φ_{mean} increase monotonically with U, while Φ_{RMS} stays nearly zero. This is therefore the static deflection regime. The second regime extends from a flow velocity of about 6 to 7 m/s where noticeable flutter first occurs. The distinct feature of this regime is that both Φ_{mean} and Φ_{RMS} increase with velocity whereas the flutter frequency f_Φ remains nearly constant. The third regime extends from a flow velocity of 7 to 10 m/s and in this regime, Φ_{mean} reaches a plateau of about 70 degrees, whereas the flutter amplitude, as measured by Φ_{RMS}, as well as the flutter frequency continue to increase, albeit slowly. The fourth

regime occurs for flow velocities greater than 10 m/s and in this regime, both the mean deflection and flutter amplitude are nearly constant but the flutter frequency continues to increase linearly. For the 0.79 mm membrane, the overall behavior is quite similar except in the fourth regime, where the flutter amplitude is observed to grow slowly but continuously. For the 0.92 mm membrane the onset of flutter occurs at a much higher velocity of 10 m/s and while there is some saturation of the mean deflection with increasing velocity, the flutter amplitude is found to increase continuously with increasing flow speed.

For the case with $\theta_Y = 45°$ we identify three distinct regimes with increasing flow speed. For the 0.62 mm membrane, during the static deflection regime that extends to a velocity of about 7 m/s, the mean deflection of the leading edge is noticeably larger than the trailing edge. In the narrow regime from 7 - 8 m/s, the membrane starts to flutter with a small (< 8º) amplitude but overall there is no significant change in the deflection of the membrane. A high variability in the flutter frequency is also observed in this regime. Between 8 and 8.5 m/s there is a dramatic change in the dynamics of the membrane: the mean deflection of the leading edge reduces rapidly to become nearly equal to that for the trailing edge and the flutter amplitude of both the leading and trailing edge increases rapidly. The flutter amplitude of the trailing-edge is observed to be significantly larger than that for the leading edge in this regime. The flutter frequency is also observed to drop rapidly in this narrow regime from about 10 Hz to about 8 Hz. Beyond about 8.5 m/s, the membrane enters its final regime where the mean deflection increases slowly with velocity and flutter frequency increases linearly. The flutter amplitude in this regime shows a more complex behavior with the amplitude of the leading edge increasing slowly but the amplitude of the trailing edge reducing slowly before becoming nearly constant.

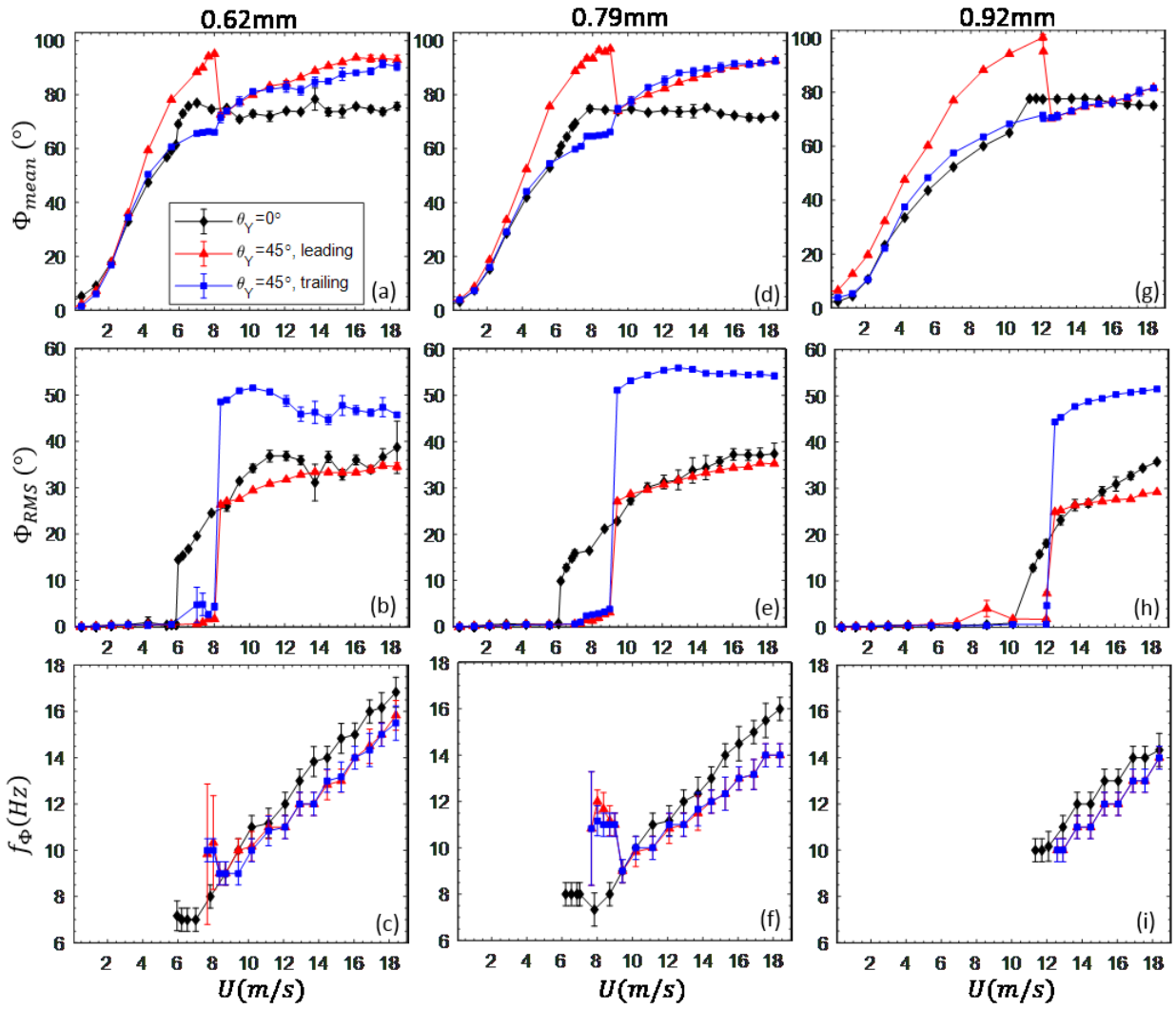

Figure 6. Membrane motion with the increase of flow velocity at $\theta_Y = 0°$ and $45°$. (a, d, g), (b, e, h), and (c, f, i) show the mean deflection Φ_{mean}, flutter amplitude Φ_{RMS} and the dominant frequency f_Θ of tip flutter, respectively. The standard deviation in the six individual experiments for each case is also shown in the plots.

For the 0.79 mm membrane, the flutter with $\theta_Y = 45°$ shows two main differences. First, the flutter onset velocity increases to about 9 m/s and secondly, the amplitude of the trailing-edge shows a simple saturation behavior at high flow velocities. The 0.92 mm membrane starts to flutter at a flow velocity of about 12 m/s and furthermore, in the third and final regime, the flutter amplitude of the trailing-edge is found to grow continuously with flow velocity within the range of flow velocities investigated here. The data associated with Fig. 6 is included in tabulated form in Appendix Table A1.

C. Effect of Membrane Shape on Critical Speed

In this section, we provide data on the critical speed (U_c) for the onset of flutter for membranes of different sizes and shapes. Figure 7 plots the critical speed of suspended membrane when $\theta_Y = 0°$. The critical speed is found to decrease gradually, as the width of the membrane is increased while holding the membrane length constant. The critical speed is also found to increase with decreasing membrane length, with a rate of increase that is significantly faster than that seen with width changes. Note that we did not obtain the critical speed when the length decreases below 40 mm due to the speed limitation of the wind tunnel. Lastly, the critical speed is also observed to increase with increase in membrane aspect-ratio (W/L), while keeping the total area constant and equal to 5625 mm^2.

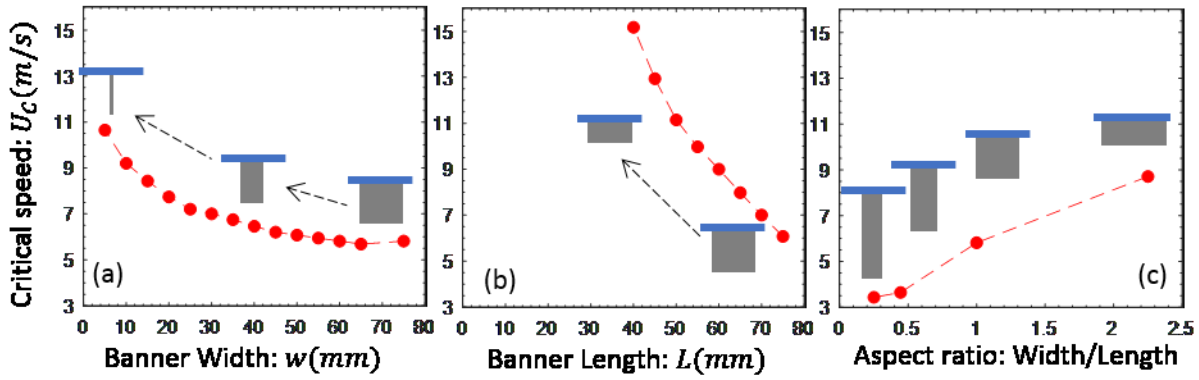

Figure 7. Membrane critical speed (Uc) as a function of membrane shape and size for $\theta_Y = 0°$. (a) Change with increasing width and fixed length; (b) change with increasing membrane length and fixed width; and (c) change with increasing membrane aspect ratio with fixed area. In these experiments, (a) and (c) use 0.62 mm membranes and (b) uses 0.79 mm membranes.

D. Scaling with Non-dimensional Parameters

It is useful to examine the scaling of the flutter dynamics in terms of appropriate dimensionless numbers. The reduced velocity $U^* = UL\sqrt{\rho_m h/k_b}$ is a well-established dimensionless number for scaling flow speed in these FSI configurations, and Fig. 8 shows the mean and RMS deflection angle plotted against U^*. As expected, there is good collapse between the curves for the membranes with different thicknesses both for the normal and yawed membranes. The critical reduced velocity for the normal membranes ranges from 65 to 85 whereas the critical reduced velocity for the yawed membrane varies over of a smaller range from 95 to 105.

For the frequency scaling, we employ a Strouhal number based on the vertical amplitude of the trailing-edge of the membrane, ie. $St = f.A_{tip}/U$. With this scaling, we find that for the normal membranes, the Strouhal numbers for all three membranes reach an asymptotic value at around U^*~150 and this asymptotic value ranges from about 0.07 for the thickest membrane to 0.12 for the thinnest membrane. For the yawed membranes, the membranes achieve nearly constant values very rapidly beyond the critical velocity and these values are also in the 0.07 - 0.12 range.

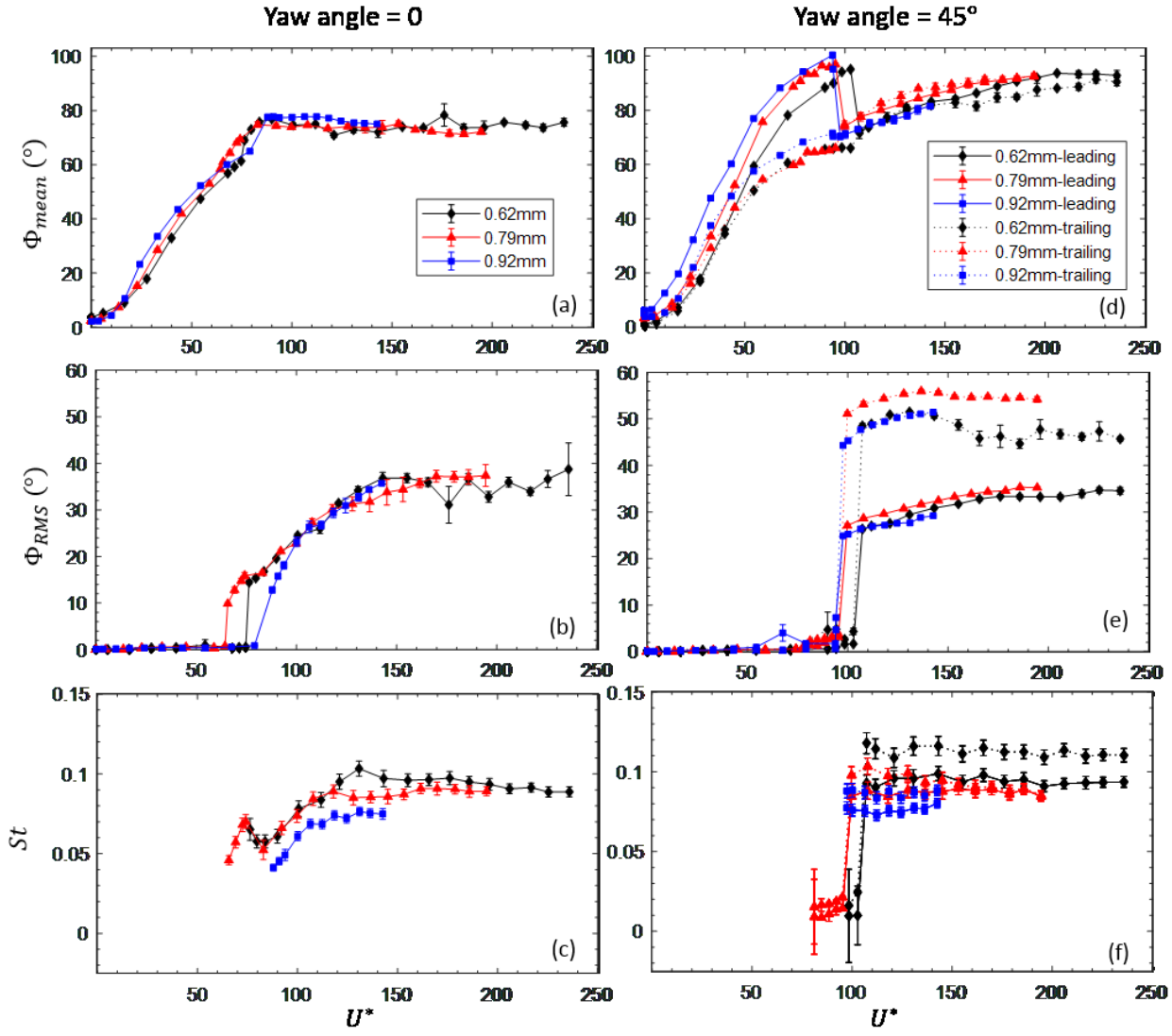

Figure 8. Membrane flutter phenomena, represented by the mean, RMS of Φ, and St number, against reduced velocity.

Finally, in Fig. 9, we compare the critical velocities U_C^* versus mass ratios for the suspended membrane with other fluttering membrane configurations [31, 43, 54, 56, 62, 64-67, 72] including regular and inverted flags/membranes. We find that in general, the inverted flags have the lowest U_C^* of all these systems with critical reduced velocities as low as about 2. However, these seem to be limited to lower mass ratios. (M^*<0.4). Conventional flags have higher critical velocities (U_C^*>6) but they occur in experiments at mass-ratios of greater than about 0.2. Finally, the suspended membrane has the highest critical velocities ($U_C^* > 65$) and the current experiments are limited to mass-ratios below 0.2. The Reynolds number for the lowest critical velocity has also been estimated for each configuration and the minimum Reynolds number at which flutter occurs (Re_C) ranges from $O(10^4)$ to $O(10^5)$. As discussed earlier, one feature that is desirable in an FIF benchmark experiment is the occurrence of flutter at relatively low (O(1000) or lower) Reynolds number, which can be resolved accurately in time-accurate flow simulations. The suspended membrane, as with the other membrane configurations, does not achieve this desired behavior.

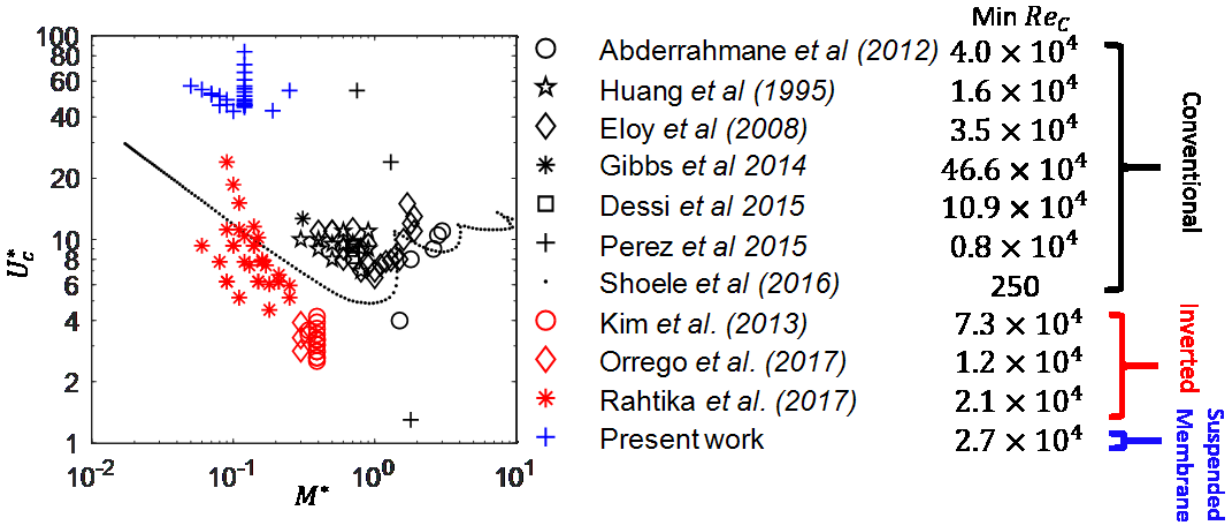

Figure 9. Overview of critical speeds of flow-induced flutter in membranes from different studies.

IV. Conclusions

There exists, a largely unmet need for experiments that can be employed for comprehensive validation of computational models of the flow-induced flutter of elastic membranes. To address this need, we have performed a

systematic experimental study on the flow-induced flutter of a suspended rectangular membrane. Using a high-speed imaging system, the envelope and tip trajectory, deflection angle, flutter intensity and flutter frequency of these suspended membranes are investigated and characterized quantitatively over a large range of flow velocities and yaw angles. The system exhibits a variety of distinct bifurcations and flutter regimes and we believe that this configuration could be useful as a benchmark for validation of computational models of flow-induced flutter of elastic membranes.

Appendix

Table A1. Raw date of Fig. 6.

Yaw Angle	Membrane	Quantities	Results																										
Yaw angle=0	0.62mm	Flow Speed (m/s)	0.0	0.5	1.3	2.2	3.1	4.2	5.3	5.6	5.8	6.0	6.2	6.5	7.0	7.8	8.7	9.4	10.2	11.2	12.1	12.9	13.7	14.5	15.3	16.1	16.9	17.6	18.4
		Mean Deflection Angle (degree)	3.7	5.2	9.1	17.9	32.9	47.4	56.8	59.2	61.4	69.1	73.0	75.7	76.9	74.6	75.0	70.9	72.9	72.0	74.0	73.6	78.3	73.6	73.8	75.7	74.6	73.7	75.6
		RMS Deflection Angle (degree)	0.0	0.1	0.1	0.4	0.5	0.9	0.4	0.5	0.6	14.5	15.4	16.8	19.6	24.5	26.0	31.4	34.2	36.8	36.8	35.9	31.1	36.6	32.8	36.0	33.9	36.6	38.7
		Frequency (Hz)										7.2	7.0	7.0	7.0	8.0	9.0	10.0	11.0	11.2	12.0	13.0	13.8	14.0	14.8	15.0	16.0	16.2	16.8
	0.79mm	Flow Speed (m/s)	0.0	0.5	1.3	2.2	3.1	4.2	5.6	6.1	6.2	6.5	6.9	7.0	7.8	8.7	9.4	10.2	11.2	12.1	12.9	13.7	14.5	15.3	16.1	16.9	17.6	18.4	
		Mean Deflection Angle (degree)	2.4	3.1	7.4	15.2	28.5	41.9	52.9	58.4	61.0	64.3	68.1	69.4	74.8	74.4	73.8	74.6	73.4	74.1	73.6	73.9	75.1	72.9	72.3	71.5	71.3	72.1	
		RMS Deflection Angle (degree)	0.1	0.1	0.1	0.4	0.6	0.6	0.5	0.8	9.9	12.8	14.8	15.9	16.4	21.2	22.8	27.3	30.1	31.3	31.7	33.8	34.4	35.7	37.2	37.1	37.1	37.4	
		Frequency (Hz)								6.3	8.0	8.0	8.0	8.0	7.3	8.0	9.0	10.0	11.0	11.2	12.0	12.3	13.0	14.0	14.5	15.0	15.5	16.0	
	0.92mm	Flow Speed (m/s)	0.0	0.5	1.3	2.2	3.1	4.2	5.6	7.0	8.7	10.2	11.3	11.7	12.1	12.9	13.7	14.5	15.3	16.1	16.9	17.6	18.4						
		Mean Deflection Angle (degree)	2.2	2.4	4.4	10.6	23.2	33.5	43.6	52.3	60.0	65.0	77.6	77.7	77.4	77.5	77.7	77.8	77.2	76.1	75.5	75.3	75.0						
		RMS Deflection Angle (degree)	0.1	0.2	0.2	0.3	0.4	0.5	0.4	0.4	0.6	0.9	12.8	15.8	18.1	23.1	26.3	26.7	29.3	30.9	32.7	34.4	35.8						
		Frequency (Hz)											10.0	10.0	10.2	11.0	12.0	12.0	13.0	13.0	14.0	14.0	14.3						
Yaw angle=45, leading	0.62mm	Flow Speed (m/s)	0.0	0.5	1.3	2.2	3.1	4.2	5.6	7.0	7.3	7.7	8.0	8.4	8.7	9.4	10.2	11.2	12.1	12.9	13.7	14.5	15.3	16.1	16.9	17.6	18.4		
		Mean Deflection Angle (degree)	0.9	2.4	7.2	17.8	36.0	59.4	78.2	88.4	90.1	94.2	95.1	72.5	73.7	77.2	80.0	83.2	84.2	86.4	88.8	90.7	92.0	93.7	93.3	93.5	92.9		
		RMS Deflection Angle (degree)	0.0	0.1	0.1	0.3	0.3	0.5	0.4	0.6	0.9	1.6	1.7	26.3	27.0	27.6	29.4	30.9	31.7	32.8	33.4	33.3	33.3	33.3	34.0	34.7	34.6		
		Frequency (Hz)										9.8	10.3	9.0	9.0	10.0	10.2	11.0	11.0	12.0	12.0	12.8	13.0	14.0	14.5	15.0	15.8		
	0.79mm	Flow Speed (m/s)	0.0	0.5	1.3	2.2	3.1	4.2	5.6	7.0	7.3	7.7	8.0	8.4	8.7	9.0	9.4	10.2	11.2	12.1	12.9	13.7	14.5	15.3	16.1	16.9	17.6	18.4	
		Mean Deflection Angle (degree)	3.7	4.2	8.6	18.7	33.5	52.4	75.7	88.7	90.8	93.4	93.4	96.5	95.9	97.0	74.0	77.6	80.0	82.3	84.5	86.1	87.5	89.6	90.4	91.3	92.0	92.7	
		RMS Deflection Angle (degree)	0.1	0.0	0.2	0.3	0.3	0.5	0.5	0.6	0.7	1.4	1.3	1.9	2.7	3.1	27.1	28.7	29.6	30.7	31.7	32.4	33.3	33.9	34.4	34.6	35.3	35.2	
		Frequency (Hz)										10.8	12.0	11.7	11.2	11.0	9.0	9.8	10.0	10.8	11.0	11.5	12.0	12.3	13.0	13.2	14.0	14.0	
	0.92mm	Flow Speed (m/s)	0.0	0.5	1.3	2.2	3.1	4.2	5.6	7.0	8.7	10.2	12.1	12.1	12.6	12.9	13.7	14.5	15.3	16.1	16.9	17.6	18.4						
		Mean Deflection Angle (degree)	6.2	6.5	12.6	19.7	32.2	47.6	60.2	77.0	88.3	94.3	100.4	95.2	70.2	71.1	72.8	74.7	75.5	76.9	77.8	80.1	81.7						
		RMS Deflection Angle (degree)	0.1	0.0	0.2	0.2	0.2	0.4	0.7	1.0	4.0	1.8	1.7	7.3	24.9	25.2	26.4	26.9	27.2	27.6	27.7	28.8	29.2						
		Frequency (Hz)													10.0	10.0	11.0	11.0	12.0	12.0	13.0	13.0	14.0						
Yaw angle=45, trailing	0.62mm	Flow Speed (m/s)	0.0	0.5	1.3	2.2	3.1	4.2	5.6	7.0	7.3	7.7	8.0	8.4	8.7	9.4	10.2	11.2	12.1	12.9	13.7	14.5	15.3	16.1	16.9	17.6	18.4		
		Mean Deflection Angle (degree)	0.5	1.5	6.0	16.8	34.4	50.4	60.6	65.6	65.9	66.2	66.0	71.5	73.9	77.4	81.1	82.0	82.9	81.6	84.8	84.9	87.6	88.2	88.7	91.4	90.5		
		RMS Deflection Angle (degree)	0.0	0.0	0.1	0.3	0.4	0.5	0.5	4.7	4.8	2.6	4.3	48.5	48.9	50.9	51.5	50.7	48.7	45.8	46.3	44.7	47.7	46.7	46.2	47.3	45.7		
		Frequency (Hz)										10.0	10.0	9.0	9.0	9.0	10.0	10.8	11.0	12.0	12.0	13.0	13.2	14.0	14.3	15.0	15.5		
	0.79mm	Flow Speed (m/s)	0.0	0.5	1.3	2.2	3.1	4.2	5.6	7.0	7.3	7.7	8.0	8.4	8.7	9.0	9.4	10.2	11.2	12.1	12.9	13.7	14.5	15.3	16.1	16.9	17.6	18.4	
		Mean Deflection Angle (degree)	3.3	3.8	7.3	15.9	29.1	44.1	54.5	59.8	60.9	64.6	64.6	64.8	65.2	66.1	74.8	77.6	82.7	85.2	88.1	88.5	89.6	90.1	91.6	91.3	91.7	92.6	
		RMS Deflection Angle (degree)	0.1	0.1	0.1	0.3	0.3	0.5	0.4	0.6	1.0	2.3	2.6	2.8	3.2	3.8	51.1	53.2	54.4	55.4	56.0	55.6	54.8	54.6	54.8	54.4	54.6	54.2	
		Frequency (Hz)										10.8	11.2	11.0	11.0	11.0	9.0	10.0	10.0	11.0	11.0	11.7	12.0	12.3	13.0	13.2	14.0	14.0	
	0.92mm	Flow Speed (m/s)	0.0	0.5	1.3	2.2	3.1	4.2	5.6	7.0	8.7	10.2	12.1	12.1	12.6	12.9	13.7	14.5	15.3	16.1	16.9	17.6	18.4						
		Mean Deflection Angle (degree)	3.9	3.8	5.3	10.6	22.0	37.5	48.3	57.6	63.4	68.3	71.6	70.3	70.6	71.1	73.0	75.2	75.8	76.4	78.1	80.3	81.5						
		RMS Deflection Angle (degree)	0.1	0.1	0.1	0.2	0.3	0.4	0.4	0.4	0.4	0.6	0.6	4.7	44.3	45.3	47.7	48.7	49.4	50.3	50.7	51.0	51.5						
		Frequency (Hz)													10.0	10.0	11.0	11.0	12.0	12.0	13.0	13.0	14.0						

Acknowledgments

The authors thank Dr. Kourosh Shoele for discussions on flow-induced flutter. We thank the support from NSF grants IIS-134477 & PHY- 1806689, and AFOSR grant FA9550-16-1-0404, monitored by Dr. Gregg Abate.

References

[1] Slone, A. K., Pericleous, K., Bailey, C., Cross, M., and Bennett, C. "A finite volume unstructured mesh approach to dynamic fluid-structure interaction: an assessment of the challenge of predicting the onset of flutter," *Applied Mathematical Modelling* Vol. 28, No. 2, 2004, pp. 211-239.

[2] dos Santos, C. R., Pereira, D. A., and Marques, F. D. "On limit cycle oscillations of typical aeroelastic section with different preset angles of incidence at low airspeeds," *Journal of Fluids and Structures* Vol. 74, 2017, pp. 19-34.

[3] Zheng, L. X., Hedrick, T. L., and Mittal, R. "A multi-fidelity modelling approach for evaluation and optimization of wing stroke aerodynamics in flapping flight," *Journal of Fluid Mechanics* Vol. 721, 2013, pp. 118-154.

[4] Zheng, L., Hedrick, T., and Mittal, R. "A comparative study of the hovering efficiency of flapping and revolving wings," *Bioinspiration & Biomimetics* Vol. 8, No. 3, 2013.

[5] Mittal, R., Erath, B. D., and Plesniak, M. W. "Fluid Dynamics of Human Phonation and Speech," *Annual Review of Fluid Mechanics, Vol 45* Vol. 45, 2013, pp. 437-467.

[6] Gilmanov, A., and Acharya, S. "A computational strategy for simulating heat transfer and flow past deformable objects," *International Journal of Heat and Mass Transfer* Vol. 51, No. 17-18, 2008, pp. 4415-4426.

[7] Shoele, K., and Mittal, R. "Energy harvesting by flow-induced flutter in a simple model of an inverted piezoelectric flag," *Journal of Fluid Mechanics* Vol. 790, 2016, pp. 582-606.

[8] Wolf, E. M., Schrock, C. R., and Wukie, N. A. "Implementation of an Arbitrary Lagrangian-Eulerian Moving Mesh Capability in the ChiDG Discontinuous Galerkin Code with Applications to Fluid-Structure Interaction," *2018 Fluid Dynamics Conference*. American Institute of Aeronautics and Astronautics, 2018.

[9] Shahriar, A., Shoele, K., and Kumar, R. "Aero-thermo-elastic Simulation of Shock-Boundary Layer Interaction over a Compliant Surface," *2018 Fluid Dynamics Conference*. American Institute of Aeronautics and Astronautics, 2018.

[10] Wang, T.-K., and Shoele, K. "Aeroelastic Flutter in the Presence of an Active Flap," *2018 Fluid Dynamics Conference*. American Institute of Aeronautics and Astronautics, 2018.

[11] Vanharen, J., Feuillet, R., and Alauzet, F. "Mesh adaptation for fluid-structure interaction problems," *2018 Fluid Dynamics Conference*. American Institute of Aeronautics and Astronautics, 2018.

[12] O'Connell, M., Druyor, C., Thompson, K. B., Jacobson, K., Anderson, W. K., Nielsen, E. J., Carlson, J.-R., Park, M. A., Jones, W. T., Biedron, R., Lee-Rausch, E. M., and Kleb, B. "Application of the Dependency Inversion Principle to Multidisciplinary Software Development," *2018 Fluid Dynamics Conference*. American Institute of Aeronautics and Astronautics, 2018.

[13] Seidel, J., Siefers, T. M., Fagley, C. P., and McLaughlin, T. E. "Large Amplitude Limit Cycle Oscillations of Fully Coupled Fluid-Structure Interactions," *2018 Fluid Dynamics Conference*. American Institute of Aeronautics and Astronautics, 2018.

[14] Vahab, M., Shoele, K., and Sussman, M. "Interaction of an Oscillating Flexible Plate and Nucleate Pool Boiling Vapor Bubble: Fluid-Structure Interaction in a Multimaterial Multiphase System," *2018 Fluid Dynamics Conference*. American Institute of Aeronautics and Astronautics, 2018.

[15] Lynch, K. P., Jones, E., and Wagner, J. L. "Simultaneous PSP and surface deformation measurements for fluid-structure interactions in a shock tube," *2018 Fluid Dynamics Conference*. American Institute of Aeronautics and Astronautics, 2018.

[16] Djeddi, R., and Ekici, K. "An Adaptive Mesh Redistribution Approach for Time-Spectral/Harmonic-Balance Flow Solvers," *2018 Fluid Dynamics Conference*. American Institute of Aeronautics and Astronautics, 2018.

[17] Seidel, J., Siefers, T. M., Fagley, C. P., and McLaughlin, T. E. "Large Amplitude Limit Cycle Oscillations of Fully Coupled Fluid-Structure Interactions," *2018 Fluid Dynamics Conference*. 2018, p. 3392.

[18] Zhu, L. D., and Peskin, C. S. "Simulation of a flapping flexible filament in a flowing soap film by the immersed boundary method," *Journal of Computational Physics* Vol. 179, No. 2, 2002, pp. 452-468.
[19] Farnell, D. J. J., David, T., and Barton, D. C. "Numerical simulations of a filament in a flowing soap film," *International Journal for Numerical Methods in Fluids* Vol. 44, No. 3, 2004, pp. 313-330.
[20] Huang, W. X., and Sung, H. J. "Three-dimensional simulation of a flapping flag in a uniform flow," *Journal of Fluid Mechanics* Vol. 653, 2010, pp. 301-336.
[21] Favier, J., Revell, A., and Pinelli, A. "A Lattice Boltzmann-Immersed Boundary method to simulate the fluid interaction with moving and slender flexible objects," *Journal of Computational Physics* Vol. 261, 2014, pp. 145-161.
[22] Favier, J., Revell, A., and Pinelli, A. "Numerical study of flapping filaments in a uniform fluid flow," *Journal of Fluids and Structures* Vol. 53, 2015, pp. 26-35.
[23] Park, S. G., Kim, B., Chang, C. B., Ryu, J., and Sung, H. J. "Enhancement of heat transfer by a self-oscillating inverted flag in a Poiseuille channel flow," *International Journal of Heat and Mass Transfer* Vol. 96, 2016, pp. 362-370.
[24] Zhang, J., Childress, S., Libchaber, A., and Shelley, M. "Flexible filaments in a flowing soap film as a model for one-dimensional flags in a two-dimensional wind," *Nature* Vol. 408, No. 6814, 2000, p. 835.
[25] Zhu, L., and Peskin, C. S. "Interaction of two flapping filaments in a flowing soap film," *Physics of Fluids* Vol. 15, No. 7, 2003, pp. 1954-1960.
[26] Farnell, D. J. J., David, T., and Barton, D. C. "Coupled states of flapping flags," *Journal of Fluids and Structures* Vol. 19, No. 1, 2004, pp. 29-36.
[27] Huang, W.-X., Shin, S. J., and Sung, H. J. "Simulation of flexible filaments in a uniform flow by the immersed boundary method," *Journal of computational physics* Vol. 226, No. 2, 2007, pp. 2206-2228.
[28] Kim, S., Huang, W. X., and Sung, H. J. "Constructive and destructive interaction modes between two tandem flexible flags in viscous flow," *Journal of Fluid Mechanics* Vol. 661, 2010, pp. 511-521.
[29] Tian, F. B., Luo, H. X., Zhu, L. D., Liao, J. C., and Lu, X. Y. "An efficient immersed boundary-lattice Boltzmann method for the hydrodynamic interaction of elastic filaments," *Journal of Computational Physics* Vol. 230, No. 19, 2011, pp. 7266-7283.
[30] Ryu, J., Park, S. G., Kim, B., and Sung, H. J. "Flapping dynamics of an inverted flag in a uniform flow," *Journal of Fluids and Structures* Vol. 57, 2015, pp. 159-169.
[31] Kim, D., Cosse, J., Cerdeira, C. H., and Gharib, M. "Flapping dynamics of an inverted flag," *Journal of Fluid Mechanics* Vol. 736, 2013.
[32] Gurugubelli, P. S., and Jaiman, R. K. "Self-induced flapping dynamics of a flexible inverted foil in a uniform flow," *Journal of Fluid Mechanics* Vol. 781, 2015, pp. 657-694.
[33] Connell, B. S. H., and Yue, D. K. P. "Flapping dynamics of a flag in a uniform stream," *Journal of Fluid Mechanics* Vol. 581, 2007, pp. 33-68.
[34] Shoele, K., and Mittal, R. "Computational study of flow-induced vibration of a reed in a channel and effect on convective heat transfer," *Physics of Fluids* Vol. 26, No. 12, 2014.
[35] Turek, S., and Hron, J. "Proposal for Numerical Benchmarking of Fluid-Structure Interaction between an Elastic Object and Laminar Incompressible Flow," *Fluid-Structure Interaction*. Springer Berlin Heidelberg, Berlin, Heidelberg, 2006, pp. 371-385.
[36] Tang, C., Liu, N. S., and Lu, X. Y. "Dynamics of an inverted flexible plate in a uniform flow," *Physics of Fluids* Vol. 27, No. 7, 2015.
[37] Dong, D. B., Chen, W. S., and Shi, S. J. "Coupling Motion and Energy Harvesting of Two Side-by-Side Flexible Plates in a 3D Uniform Flow," *Applied Sciences-Basel* Vol. 6, No. 5, 2016.
[38] Gilmanov, A., Le, T. B., and Sotiropoulos, F. "A numerical approach for simulating fluid structure interaction of flexible thin shells undergoing arbitrarily large deformations in complex domains," *Journal of Computational Physics* Vol. 300, 2015, pp. 814-843.
[39] Taneda, S. "Waving motions of flags," *Journal of the Physical Society of Japan* Vol. 24, No. 2, 1968, pp. 392-401.
[40] Yamaguchi, N., Sekiguchi, T., Yokota, K., and Tsujimoto, Y. "Flutter limits and behavior of a flexible thin sheet in high-speed flow—II: experimental results and predicted behaviors for low mass ratios," *Journal of fluids engineering* Vol. 122, No. 1, 2000, pp. 74-83.
[41] Balint, T. S., and Lucey, A. D. "Instability of a cantilevered flexible plate in viscous channel flow," *Journal of Fluids and Structures* Vol. 20, No. 7, 2005, pp. 893-912.

[42] Tang, L., and Paidoussis, M. P. "On the instability and the post-critical behaviour of two-dimensional cantilevered flexible plate's in axial flow," *Journal of Sound and Vibration* Vol. 305, No. 1-2, 2007, pp. 97-115.
[43] Eloy, C., Lagrange, R., Souilliez, C., and Schouveiler, L. "Aeroelastic instability of cantilevered flexible plates in uniform flow," *Journal of Fluid Mechanics* Vol. 611, 2008, pp. 97-106.
[44] Pang, Z., Jia, L. B., and Yin, X. Z. "Flutter instability of rectangle and trapezoid flags in uniform flow," *Physics of Fluids* Vol. 22, No. 12, 2010.
[45] Bryant, M., Wolff, E., and Garcia, E. "Aeroelastic flutter energy harvester design: the sensitivity of the driving instability to system parameters," *Smart Materials & Structures* Vol. 20, No. 12, 2011.
[46] Eloy, C., Kofman, N., and Schouveiler, L. "The origin of hysteresis in the flag instability," *Journal of Fluid Mechanics* Vol. 691, 2012, pp. 583-593.
[47] Allen, J. J., and Smits, A. J. "ENERGY HARVESTING EEL," *Journal of Fluids and Structures* Vol. 15, No. 3, 2001, pp. 629-640.
[48] Giacomello, A., and Porfiri, M. "Energy harvesting from flutter instabilities of heavy flags in water through ionic polymer metal composites," *Electroactive Polymer Actuators and Devices (Eapad) 2011* Vol. 7976, 2011.
[49] Bryant, M., Mahtani, R. L., and Garcia, E. "Wake synergies enhance performance in aeroelastic vibration energy harvesting," *Journal of Intelligent Material Systems and Structures* Vol. 23, No. 10, 2012, pp. 1131-1141.
[50] Akcabay, D. T., and Young, Y. L. "Hydroelastic response and energy harvesting potential of flexible piezoelectric beams in viscous flow," *Physics of Fluids* Vol. 24, No. 5, 2012.
[51] Michelin, S., and Doare, O. "Energy harvesting efficiency of piezoelectric flags in axial flows," *Journal of Fluid Mechanics* Vol. 714, 2013, pp. 489-504.
[52] Deivasigamani, A., McCarthy, J. M., John, S., Watkins, S., and Coman, F. "Investigation of Asymmetrical Configurations for Piezoelectric Energy Harvesting from Fluid Flow," *Proceedings of the Asme Conference on Smart Materials Adaptive Structures and Intelligent Systems, 2014, Vol 2*, 2014.
[53] Kirschmeier, B., and Bryant, M. "Soap film flow visualization investigation of oscillating wing energy harvesters," *Bioinspiration, Biomimetics, and Bioreplication 2015* Vol. 9429, 2015.
[54] Perez, M., Boisseau, S., Gasnier, P., Willemin, J., and Reboud, J. L. "An electret-based aeroelastic flutter energy harvester," *Smart Materials and Structures* Vol. 24, No. 3, 2015.
[55] Bernitsas, M. M. "Harvesting Energy by Flow Included Motions," *Springer Handbook of Ocean Engineering*, 2016, pp. 1163-1244.
[56] Orrego, S., Shoele, K., Ruas, A., Doran, K., Caggiano, B., Mittal, R., and Kang, S. H. "Harvesting ambient wind energy with an inverted piezoelectric flag," *Applied Energy* Vol. 194, 2017, pp. 212-222.
[57] Vogel, S. "Drag and Reconfiguration of Broad Leaves in High Winds," *Journal of Experimental Botany* Vol. 40, No. 8, 1989, pp. 941-948.
[58] Stewart, H. L. "Hydrodynamic consequences of flexural stiffness and buoyancy for seaweeds: a study using physical models," *Journal of Experimental Biology* Vol. 209, No. 11, 2006, p. 2170.
[59] Koehl, M. A. R. "How Do Benthic Organisms Withstand Moving Water?1," *American Zoologist* Vol. 24, No. 1, 1984, pp. 57-70.
[60] Peng, J., and Alben, S. "Effects of shape and stroke parameters on the propulsion performance of an axisymmetric swimmer," *Bioinspiration & Biomimetics* Vol. 7, No. 1, 2012, p. 016012.
[61] Sader, J. E., Cosse, J., Kim, D., Fan, B., and Gharib, M. "Large-amplitude flapping of an inverted flag in a uniform steady flow - a vortex-induced vibration," *Journal of Fluid Mechanics* Vol. 793, 2016, pp. 524-555.
[62] Kim, H., Kang, S., and Kim, D. "Dynamics of a flag behind a bluff body," *Journal of Fluids and Structures* Vol. 71, 2017, pp. 1-14.
[63] Huang, H. B., Wei, H., and Lu, X. Y. "Coupling performance of tandem flexible inverted flags in a uniform flow," *Journal of Fluid Mechanics* Vol. 837, 2018, pp. 461-476.
[64] Abderrahmane, H. A., Paidoussis, M. P., Fayed, M., and Ng, H. D. "Nonlinear dynamics of silk and Mylar flags flapping in axial flow," *Journal of Wind Engineering and Industrial Aerodynamics* Vol. 107, 2012, pp. 225-236.
[65] Huang, L. "Flutter of Cantilevered Plates in Axial-Flow," *Journal of Fluids and Structures* Vol. 9, No. 2, 1995, pp. 127-147.
[66] Gibbs, S. C., Sethna, A., Wang, I., Tang, D., and Dowell, E. "Aeroelastic stability of a cantilevered plate in yawed subsonic flow," *Journal of Fluids and Structures* Vol. 49, 2014, pp. 450-462.

[67] Dessi, D., and Mazzocconi, S. "Aeroelastic behavior of a flag in ground effect," *Journal of Fluids and Structures* Vol. 55, 2015, pp. 303-323.
[68] Meyers, M., and Chawla, K. *Mechanical behavior of materials*: Cambridge University Press, 2008.
[69] Dou, Z., Ireland, P. J., Bragg, A. D., Liang, Z., Collins, L. R., and Meng, H. "Particle-pair relative velocity measurement in high-Reynolds-number homogeneous and isotropic turbulence using 4-frame particle tracking velocimetry," *Experiments in Fluids* Vol. 59, No. 2, 2018.
[70] Dou, Z., Bragg, A. D., Hammond, A. L., Liang, Z., Collins, L. R., and Meng, H. "Effects of Reynolds number and Stokes number on particle-pair relative velocity in isotropic turbulence: a systematic experimental study," *Journal of Fluid Mechanics* Vol. 839, 2018, pp. 271-292.
[71] Dou, Z., Rips, A., Welsh, N., Seo, J.-H., and Mittal, R. "Flow-Induced Flutter of Hanging Banners: Experiments and Validated Computational Models," *2018 Fluid Dynamics Conference*. American Institute of Aeronautics and Astronautics, 2018.
[72] Rahtika, I. P. G. S., Wardana, I. N. G., Sonief, A. A., and Siswanto, E. "Experimental Investigation on Flutter Similitude of Thin-Flat Plates," *Advances in Acoustics and Vibration*, 2017, pp. 1-8.